Experimental investigation on the structural response
of RC slabs subjected to combined fire and blast

Matteo Colombo[a], Paolo Martinelli[a]*, Assis Arano[b], Jan Arve Øverli[b],

Max A.N. Hendriks[b,c], Terje Kanstad[b], Marco di Prisco[a]

[a] *Politecnico di Milano, Department of Civil and Environmental Engineering, Piazza L. da Vinci 32, 20133 Milan, Italy*

[b] *Norwegian University of Science and Technology, Department of Structural Engineering, NO-7491 Trondheim, Norway*

[c] *Technical University of Delft, Faculty of Civil Engineering and Geosciences, Stevinweg 1, Delft, Netherlands*

ABSTRACT

Reinforced concrete (RC) submerged floating tunnels (SFTs) represent a possible solution for crossing wide, deep fjords, and is considered for the E39 highway route along the Norwegian west coast. With regard to SFTs, the specific accidental scenario that is under investigation is the combined action of fire and subsequent internal explosion, as this is a crucial safety design condition for this type of structure. To assess the structural performance of reinforced concrete structures under combined fire and blast actions, gas burner equipment and a shock tube device were used to generate high temperature and blast loading, respectively, on circular RC slabs. A proper set of instruments consisting of thermocouples embedded in the specimens, accelerometers and ultrasonic pulse velocity (UPV) equipment made it possible to capture the behaviour of the slabs under the combined fire and blast actions and to distinguish the specific role of fire and blast. Simplified numerical tools such as an equivalent elastic single degree of freedom (SDOF) model and a linear elastic finite element (FE) model were used to interpret the experimental results. By considering all combinations of three fire exposure times and two shock waves, the effect of damage accumulation from a combined action of fire and subsequent internal explosion was mapped. A reliable benchmark for numerical models was obtained.

* Corresponding author at: Politecnico di Milano, Department of Civil and Environmental Engineering, Piazza L. da Vinci 32, 20133 Milan, Italy.
E-mail addresses: matteo.colombo@polimi.it (M. Colombo), paolo.martinelli@polimi.it (P. Martinelli), assis.arano@ntnu.no (A. Arano), jan.overli@ntnu.no (J. A. Øverli), max.hendriks@ntnu.no (M.A.N. Hendriks), terje.kanstad@ntnu.no (T. Kanstad), marco.diprisco@polimi.it (M. di Prisco).

1 INTRODUCTION

Tunnels represent one of the most critical infrastructures in the whole transport network of Europe. Their fragility when exposed to exceptional events like fire and/or explosion is a crucial point in the robustness of a wider transport system, from damage of the infrastructure itself to a more far-reaching domino effect, propagating consequences over a wider region due to the tunnel closure. Tunnels are bottlenecks in transport networks that can threaten the overall robustness of the system, because the breakdown of those single components can lead to the complete collapse of the transportation infrastructure. From this point of view, a capacity design approach should be adopted to minimize the failure probability of the critical points.

Disastrous events that occurred in European road tunnels, such as those of the Mont Blanc Tunnel (1999), the Gotthard Tunnel (2001), the Tauern Tunnel (2002) and the Frejus Tunnel (2005), increased attention paid to safety issues in tunnels and underlined the importance of these infrastructures from human, economic and cultural points of views.

Fire has been regarded as the main physical threat in the design of a tunnel and a wide range of research activities including experimental tests, modelling methods and design approaches have been devoted to the investigation of this problem [1][2][3][4][5][6][7][8][9][10][11][12][13][14][15]. However, nowadays, fire cannot be regarded as the only extreme accidental action: recent terroristic attacks have raised the doubt that tunnel infrastructures can also be regarded as critical targets, not only for significant life losses, but also for the huge overall costs to society, that critical damage to this kind of infrastructure can induce. Over the last decade, several researchers started to examine the behaviour of tunnels (particularly metro tunnels) subjected to internal explosion encompassing both simplified and refined numerical models [16][17][18][19][20][21][22][23][24][25]. At present, there are no experimental studies reported in literature on the topic of tunnels subjected to internal blast loads.

The research presented in this paper concerns the preliminary design of the submerged-floating tunnel (SFT), or "Archimede bridge", or Submerged Floating Tube (SFT) Bridge, that is planned for crossing Norwegian fjords. The Norwegian Public Roads Administration's Ferry-free coastal route E39 project aims to establish a coastal highway route, approximately 1100 km long, between Kristiansand and Trondheim without ferry connections. The wide, deep fjords along the Norwegian coast require new large structures to be built, and SFT is a realistic alternative [26].

The tunnel will be suspended approximately 30 m under the water's surface. The structure will comprise two tubes fixed to floating pontoons with a gap of approximately 250 m. This design allows ships to sail freely over

63   the structure, while submarines can cross underneath it. With regard to SFTs, a specific accident scenario that is

64   under investigation is the combined action of fire and subsequent internal explosion, as this is a crucial safety

65   design condition for this structure. The tragic collision of two trucks on the Casalecchio (close to Bologna, Italy)

66   junction of the A14 highway that occurred on August 6th 2018 can be regarded as an example of this kind of

67   scenario: both trucks loaded with flammable materials (GPL and chemical solvents) triggered a chain of

68   explosions that gutted the overpass, causing two deaths and 145 injuries. A recent study conducted by

69   Kristoffersen et al. [23] analysed the response of SFTs with circular and rectangular cross-sections, subjected to

70   internal explosion without fire using a finite element (FE) approach.

71   With reference to reinforced concrete (RC) structures, limited research is available in literature on the

72   combined effects of fire and blast loads and is mostly confined to numerical studies. Kakogiannis et al. [27] and

73   Pascualena et al. [28] reported the analysis of the blast bearing capacity of reinforced concrete hollow core slabs

74   when they are subjected first to fire and then to a blast load. The blast response of the hollow core slab was

75   assessed numerically in [28] and both numerically and experimentally in [27]. A numerical investigation into

76   dynamic responses of RC columns subjected to fire and blast was proposed by Ruan et al. [29]. Zhai et al. [30]

77   reported an experimental and numerical investigation of RC beams subjected to a blast after exposure to fire. A

78   prestressed concrete panel is numerically evaluated under impact-blast-fire combined loading scenarios using an

79   FE approach. Moving the attention to tunnels, the response behaviour of the tunnel lining under the action of

80   vehicle impact and fire load has been numerically analysed [31]. A numerical simplified procedure was proposed

81   by Colombo et al. [32] for the response behaviour of underground tunnels subjected to combined fire and internal

82   explosion.

83   The work presented here aims to define a reliable benchmark for the numerical model that will be instrumental

84   for the design of the tunnel under exceptional load conditions, by assessing the blast load-bearing resistance of

85   RC slabs subjected to high temperatures. For this purpose, a comprehensive experimental program was carried

86   out at Politecnico di Milano in conjunction with the Norwegian University of Science and Technology (NTNU),

87   adopting a shock tube and gas burner equipment, able to apply a fire and blast sequence [33]. The work presented

88   in this study is part of a larger research programme in which static slab tests and material tests, have been

89   performed for further understanding of the slab's behaviour [34].

90   The structural response of circular RC slabs subjected to shock wave load conditions was investigated in

91   residual conditions, after being exposed to a fire curve. According to [35], a hydrocarbon fire curve, typical of

92   tunnel designing, was first applied to five specimens. Two fire exposure times were considered (t = 60 and 120

93   min) in addition to the reference case (t=0 min). The same guideline [35] indicates t = 120 min as the fire exposure

94   time in the case of a tunnel that is a primary structure, with truck/tanker type traffic.

95   Two different shock wave loading conditions were taken into account: a "low pressure" condition (LP)

96   characterized by an incident shock wave travelling at a velocity about 1.5 Mach and a maximum reflected pressure

97   of about 400 kPa and a "High Pressure" condition (HP) characterized by an incident shock wave travelling at a

98   velocity of about 2 Mach and a maximum reflected pressure of 1100 kPa.

99   Thermocouples embedded in the specimens made it possible to measure the temperature distribution through

100   the thickness of the specimens during the fire application, whilst accelerometers, applied to the back of the slab

101   during the shock tube tests, made it possible to measure the acceleration at several points of the specimens.

102   Moreover, ultrasonic pulse-wave velocity (UPV) measurements were acquired, before and after the fire tests and

103   also after the shock tube tests, in order to quantify the decrease of the cross-section stiffness caused by both the

104   fire exposure and the shock wave application.

105   2   EXPERIMENTAL PROGRAMME

106   In this work, seven circular RC slabs were subjected to combined fire and shock wave loads. An overview of the

107   whole experimental programme is presented in Sect. 2.1. A description of the materials composing the specimens

108   (i.e. concrete and steel) is given in Sect. 2.2. The specimen's geometry and the instrumentation are presented in

109   Sect. 2.3.

110   2.1   Test programme

111   In total 7 specimens were tested in this study, of which 5 were tested under combined fire and shock wave loads.

112   Two specimens were tested under blast conditions only. **Table 1** summarizes the whole set of tests performed. In

113   all the tests, exposure to fire (if applied) always preceded the blast load.

114

Table 1 Summary of the experimental programme

Specimen ID	UPV test	fire exposition			blast test	
		0 min	60 min	120 min	low pressure	high pressure
LP0	Y	Y	-	-	Y	-
LP60	Y	-	Y	-	Y	-
LP120	Y	-	-	Y	Y	-
HP0	Y	Y	-	-	-	Y
HP60	Y	-	Y	-	-	Y
HP120-1	Y	-	-	Y	-	Y
HP120-2	Y	-	-	Y	-	Y

The experimental tests differ in terms of the reflected pressure history applied to the specimens and the time exposition at the fire curve eventually applied before the blast. Three tests, hereafter indicated as the low-pressure tests, are characterised by an average peak pressure of 370 kPa and an average specific impulse of 3386 kPa×ms. The other four tests, hereafter indicated as the high-pressure experiments, are characterised by an average peak pressure of 1111 kPa and an average specific impulse of 6241 kPa×ms. This study considers two different fire exposure times (t = 60 min and t = 120 min), in addition to the non-heated condition (t = 0 min). An abbreviation is used to indicate different tests that correspond to different specimens (for example HP120-1): LP or HP at the beginning of the abbreviation stand for low and high pressure tests, 0, 60 and 120 stand for the exposure time in minutes where 0 means that specimen was not exposed to fire, while the eventual ascending number at the end of the abbreviation identifies nominally identical specimens.

In all the tests, direct ultrasonic pulse velocity (UPV) measurements were performed before and after the fire tests and before and after the blast tests in order to quantify the internal damage produced by the combined effect of thermal exposure and blast load through the thickness of the specimen.

2.2 Materials

2.2.1 *Concrete*

A detailed and comprehensive discussion of the mechanical properties of the concrete used for the RC slabs is given in [34]. Mechanical properties of concrete were evaluated at ambient and high temperatures. Only the main points of interest are summarized in the following description.

The concrete mix design ordered as a C45/55 grade is listed in **Table 2**. The concrete compressive strength (f_c) measured on cylinders ($D = 100$ mm and $H = 200$ mm) was equal to 73 MPa. The concrete cylinders were

demoulded 24 hours after casting, cured in water for 28 days, and rested for five/six months at 20 °C in a lab

environment. The density (ρ) at 28 days was equal to 2370 kg/m^3. The concrete has a water-cement ratio (w/c) of

0.42, and a maximum aggregate size (d_{max}) of 16 mm. The siliceous aggregates were composed of granite, gneiss,

sandstone and siltstone. Polypropylene microfibres were also added into the mix (1 kg/m^3) to prevent explosive

spalling.

A set of quasi-static concrete tests, namely uniaxial compression test (UCT) and uniaxial direct tensile test

(UTT) was carried out to assess the mechanical material properties of concrete at four different temperatures.

Twelve standard cylinders (100×200 mm) were tested in uniaxial compression, measuring the modulus of

elasticity as indicated in [36] and the compressive strength. Three nominally identical specimens were tested at

different temperature levels (20, 200, 400, and 600 °C), in residual conditions. Eight cylinders (100×100 mm)

were tested in uniaxial tension with hinged end-platens by controlling the crack opening displacement (COD).

Two nominally identical specimens were tested in residual conditions at different temperature levels (20, 200,

400, and 600 °C). Further details on the material test set-up, specimen sizes and instrumentation can also be found

in [34].

Table 2 Concrete mix design

Component	Content (kg/m^3)
CEM II/B-M 42.5R	223.40
CEM II/A-V 42.5N	193.33
Silica fume	12.89
Water	174.13
Aggregate 8–16	754.95
Aggregate 0–8	1026.48
Acrylic superplasticizer	3.06
Set-retarding admixture	0.64
Polypropylene fibres	1.00

The average modulus of elasticity from the three tests at 20 °C, and its standard deviation were equal to $E_{c,20} = 27609 \pm 829$ MPa. A significant decrease in the modulus of elasticity in concrete subjected to high temperature

was observed. On average, from 20 to 200 °C, the modulus slightly reduces until $0.90E_{c,20}$. Between 200–400 °C

and 400–600 °C, the material suffers a faster reduction, reaching $0.50E_{c,20}$ and $0.20E_{c,20}$, respectively.

The average compressive peak strength from the three tests at 20 °C, and its standard deviation were equal to

$f_{c,20} = 73.00 \pm 2.44$ MPa. The compressive strength of concrete was significantly reduced due to the exposure

159　to elevated temperatures, with a trend similar to that observed for the modulus of elasticity. After exposure to

160　elevated temperatures, the residual peak strength decreases to approximately $0.90f_{c,20}$ after 200 °C, $0.50f_{c,20}$

161　after 400 °C, and $0.30f_{c,20}$ after 600 °C.

162　　　The average peak tensile strength from the two tests at 20 °C, and its standard deviation were equal to $f_{ct,20} =$

163　3.62 ± 0.56 MPa. The maximum stress reached at 200 °C is about 20% higher than the maximum stress at 20 °C.

164　Above 200 °C, the residual peak tensile strength significantly decreases to approximately $0.70f_{ct,20}$ for 400 °C

165　and $0.30f_{ct,20}$ for 600 °C. Complete stress-strain and stress-COD curves were measured during the UCTs and

166　UTTs, in addition to peak compressive strength and peak tensile strength, but are omitted here for the sake of

167　brevity. A detailed and comprehensive discussion of the mechanical properties of concrete exposed to high

168　temperatures is given in [34].

169　*2.2.2　Steel*

170　Traditional B450 steel with Ø6 mm rebars were used to prepare the circular RC slabs. Eight steel reinforcing bars

171　were tested in uniaxial tension according to [37], using an INSTRON machine with a maximum capacity of 200

172　kN. The tests were carried out under displacement control by means of a high-accuracy transducer, with a gauge

173　length of 50 mm, placed at the central part measuring the elongation of the rebar until it reached 2%. An internal

174　transducer of the machine was then used to follow the test until complete failure of the specimen. Two nominally

175　identical specimens were tested, in residual conditions at different temperature levels (20, 200, 400, and 600 °C).

176　By controlling the displacement, complete stress-strain curves were measured during the tests, in addition to

177　yielding and ultimate strengths. After the tests, the elongation at failure was measured according to [37]. The

178　average yielding strength for the steel rebar at room temperature is $f_{y,20} = 500.85$ MPa. The average ultimate

179　strength and strain at room temperature are $f_{t,20} = 648.77$ MPa and $\varepsilon_{su,20} = 0.328$, respectively. The mechanical

180　properties at high temperatures experienced a strong recovery during the cooling phase. The yielding and ultimate

181　strength after exposure to 600°C were very similar to those for the non-heated specimens.

182　**2.3　Specimen geometry and instrumentation**

183　The slab specimens consist of circular reinforced concrete slabs, 70 mm thick, with a diameter of 690 mm. Two

184　layers of bi-directional reinforcement (Ø6/60mm both in x and y direction) were positioned as shown in **Figure**

185　**1**. A net concrete cover of 10 mm was used. The specimen sizes are detailed in **Figure 1**.
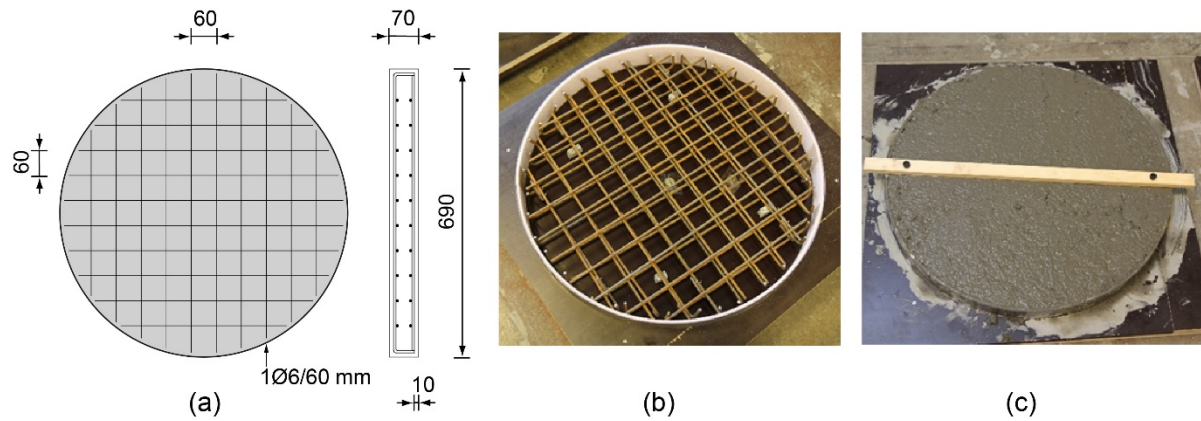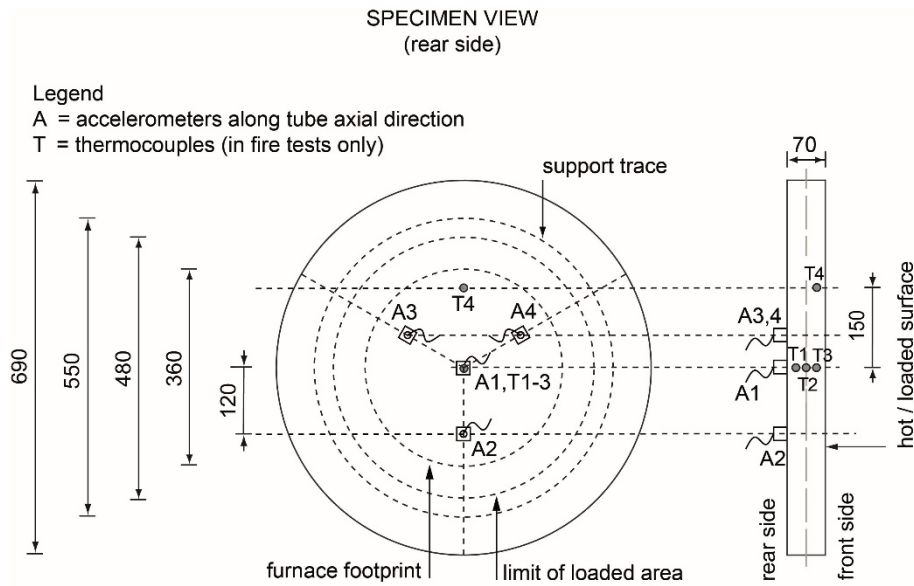
Figure 1 Reinforced concrete slab specimen: (a) specimen size, (b) mould used to cast the slab and (c) view of the cast slab (units: mm)

186   The specimen's geometry was mainly dictated by the dimensions of the shock tube equipment. In addition,

187   the thickness and reinforcement ratio were determined in order to ensure a linear elastic behaviour of the slab

188   under the reference load conditions (test LP0). An elastic analytical computation of the slab [38], considering not

189   thermally damaged material, provides a pressure corresponding to the first cracking (p_{cr}) in static condition equal

190   to 400 kPa, while the ultimate pressure (p_u) computed according to a yield line approach [39] for static condition

191   is equal to 1100 kPa.

192   The specimen's acceleration along the shock tube axis (out-of-plane slab acceleration) was measured by means

193   of four ICP (Integrate Circuit Piezoelectric) accelerometers: one (A1) placed at the specimen's centre and the

194   other three (A2–A4) placed at relative angular positions of 120° at 120 mm from the specimen's centre (**Figure**

195   **2**). A fifth accelerometer (A5) was mounted on the shock tube at the end of the driven chamber to record the axial

196   accelerations of the device (**Figure 6** and **Figure 7b**). The accelerometer characteristics are: a quartz sensing

197   element with a measuring range of ±500 g pk (peak acceleration), a band width larger than 10 kHz, a broadband

198   resolution of 0.005 g rms (root mean square) and a resonant frequency higher than 70 kHz.

SPECIMEN VIEW
(rear side)

Legend
A = accelerometers along tube axial direction
T = thermocouples (in fire tests only)

Figure 2 Instrumentation installed on the specimen (units: mm)

199   A set of three ICP dynamic pressure sensors was positioned along the tube's axis as indicated in **Figure 6**. The

200   pressure sensors (PT1-PT3) have a quartz sensing element with a full-scale pressure of 6.9 MPa, a sensitivity of

201   0.7 mV/kPa, a rise time lower than 1 μs and a resonant frequency higher than 500 kHz. The signal conditioning

202   for both accelerometers and pressure sensors mounted on the shock tube (see Sect. 3.3 for its description) is

203   performed with an ICP signal conditioner with gain equal to one, a bandwidth equal to 10 kHz and a broadband

204   electrical noise equal to 3.5 μV rms. All channels are acquired by means of the same data acquisition system with

205   56 parallel channels with the maximum sampling rate of 3 MS/s per channel and a 14-bit resolution. The data

206   acquisition for all the channels is triggered by the signal of the pressure sensor PT1 placed at a distance of 2250

207   mm from the driven end flange: when the shock wave goes through its position, the system starts acquiring data

208   with a sampling rate of 1 MS/s.

209   Specimens exposed to high temperatures were instrumented with four thermocouples each. Type-K

210   chromel/alumel thermocouples (0.91 mm thick) were installed during fabrication at three different depths in the

211   specimen. Thermocouples T1-T3 were located at the centre of the specimen at 16, 35 and 54 mm from the "hot

212   surface", respectively, for measuring the concrete temperature through the thickness. Thermocouple T4 is located

213   at 150 mm from the centre along the radial direction at a depth of 16 mm from the "hot surface" (see **Figure 2**).

214   **3   DESCRIPTION OF SLAB TESTS**

215   The tests were conducted according to the following sequence: (a) application of UPV tests on virgin specimen,

216   (b) application of the fire curve with exposure time equal to t = 60 min or t = 120 min, (c) UPV measurements for

217 evaluation of fire damage, (d) application of low or high pressure blast tests and (e) UPV measurements for the

218 assessment of combined fire and blast damage. Tests where high-temperature exposure was not applied (t = 0

219 min) served as reference tests; in these cases phases (b) and (c) were not applied. The description of UPV

220 measurements, fire tests and blast tests is given in Sections 3.1-3.3.

3.1 UPV measurements

222 Direct UPV measurements [40] were carried out on the specimens before and after the fire and blast tests. The

223 aim of these measurements was to quantify the internal damage produced by the thermal exposure and by the blast

224 load through the thickness of each specimen. The emitting and receiving probes were placed on opposite specimen

225 faces since a direct UPV method was adopted. Six points were monitored: points U1-U3 were located at a distance

226 of 50 mm from the specimen's centre, whereas points U4-U6 were located at a distance of 170 mm (see **Figure**

227 **3**). Gel was used to avoid air between the transducer and the specimen's surface.
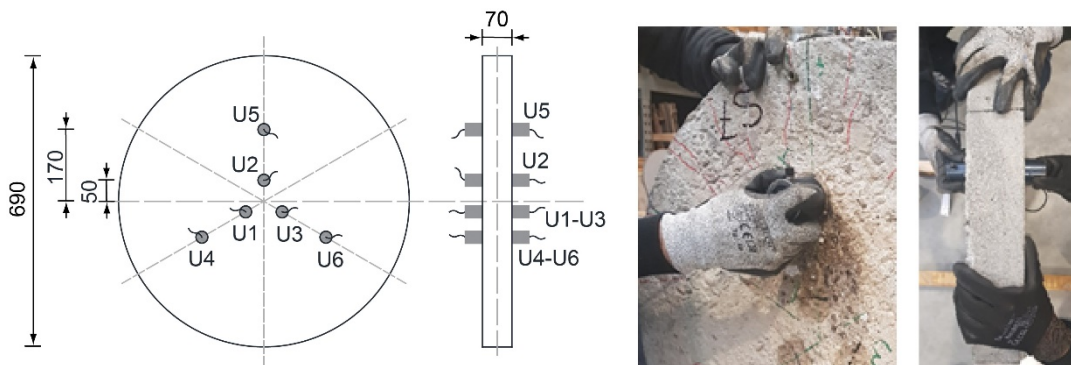
**Figure 3** Direct UPV measurements on RC slab specimen (units: mm)

3.2 Fire exposure

229 The fire curve was applied to the specimens by means of a gas burner. The burner equipment comprises a nozzle

230 mix burner in which gas and air are mixed at the point of discharge. The burner is mounted by means of a proper

231 flange to a chamber in which the burning process takes place. The chamber is designed to allow proper smoke

232 evacuation and it is closed on one side by the specimen itself in order to heat the specimen's surface. A

233 hydrocarbon curve [14], typical of accidents in tunnels, was applied on one face of the specimen (the free surface

234 during casting) on a circular area with a diameter equal to 360 mm (**Figure 4**). A thermal sensor installed inside

235 the burner makes it possible to automatically regulate the intensity of the flame to achieve the desired temperature

236 vs time curve (i.e. fire curve). Two different high temperature exposure times, t = 60 min and t = 120 min, were

237 considered. The fire curves recorded during the fire tests are shown in **Figure 5** and compared with the target

238 hydrocarbon fire curve. The specimens were allowed to expand freely due to increase of temperature during the

239 test. Once the desired exposure time was reached, the burner was turned off and the specimens cooled naturally

240 in the free laboratory environment. During the LP60 test there was a problem in following the target temperature.

241 The problem was solved during the other tests and did not have any impact on the results that are presented in

242 Sect. 4.

243   All specimens subjected to the fire curve were instrumented with four thermocouples for measuring the

244 concrete temperature through the thickness (see Sect. 2.3 for the description of the instrumentation). Despite the

245 addition of polypropylene microfibers in the concrete matrix, minor explosive spalling occurred during the first

246 minutes of all the tests subjected to fire exposure. Nevertheless, this phenomenon was limited to a small region of

247 the specimen and with a maximum depth close to the concrete cover (c = 10 mm). The region characterized by

248 the spalling phenomenon is highlighted as a grey region in **Figure 13**.

249
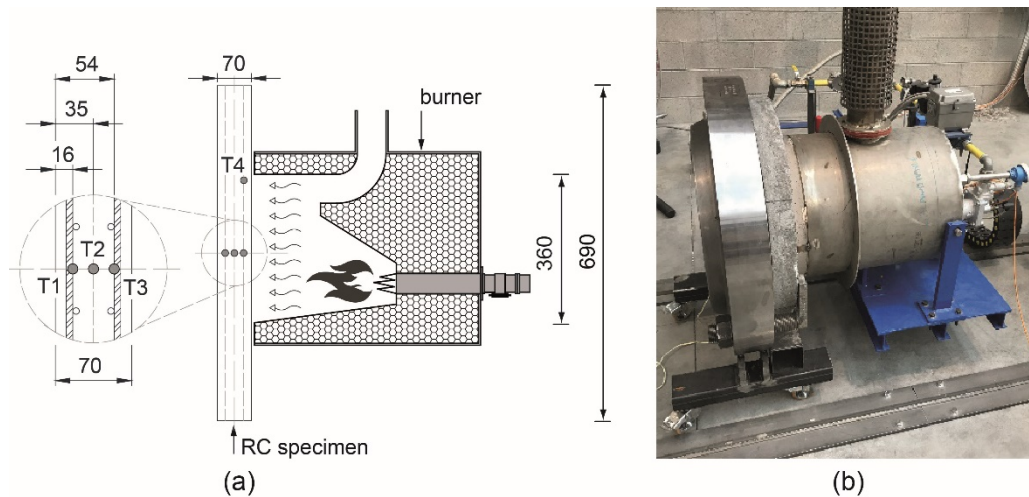
Figure 4 Fire curve application: (a) schematic view of the burner equipment and (b) picture of the burner and of the specimen ready for the fire test (units: mm)
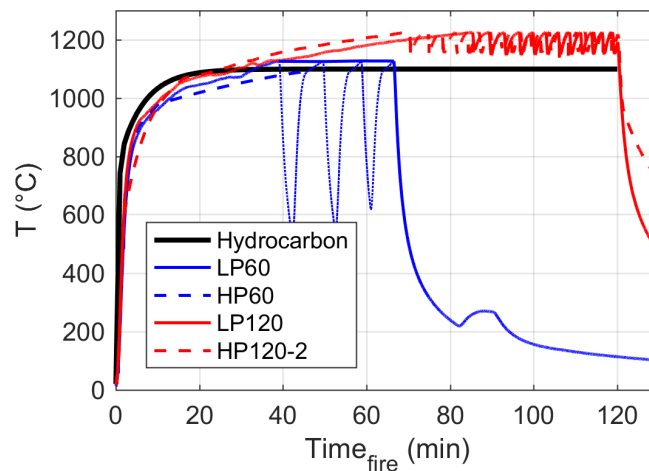
**Figure 5** Recorded and target fire curves

11

3.3 Blast tests

The blast tests were carried out at Politecnico di Milano by adopting a double diaphragm shock tube facility. The shock tube was used as blast simulator; the idea to use shock tubes to simulate blast loading on structures is not new and this technique was developed to reproduce blast waves nearly identical to those obtained in live explosive tests [41][42]. Examples of the use of shock tubes to analyse the dynamic behaviour of concrete slabs and RC slabs according to several boundary conditions, like simply supported/clamped or resting on the ground can be found in [43][44][45].

The shock tube was originally adopted to investigate the behaviour of underground tunnel linings under blast conditions [45][46] through the use of an ad-hoc chamber designed to investigate soil-structure interaction. The shock tube was easily adapted to study plates under blast loads with different boundary conditions by changing the end chamber. The shock tube is able to produce a high-pressure loading range, with a maximum reflected target pressure of about 3000 kPa. A detailed description of all the shock tube's components can be found in [33], while a comprehensive discussion on the shock tube's performance is given in [47]; only the main points of interest are summarized below.

Figure 6 shows a schematic layout of the shock tube device in the assembled configuration. It consists of three chambers that can move on a linear guide system: the driver chamber, the diaphragm chamber (i.e. firing section or buffer chamber) and the driven chamber. The test area in which the specimen is fixed is placed at the end of the driven chamber. The tests were carried out using pressurized helium inside the driver and buffer chambers, and air at ambient condition in the driven chamber.

Driver, buffer and driven chambers have a length of 2.35, 0.26 and 10.5 m, respectively, thus resulting in a total shock tube length, excluding the test area, of 13.11 m. The driver and driven chambers have a 13.5 mm thick wall, while the buffer chamber has an external diameter of 857 mm that corresponds to the maximum diameter of the flange welded on the driver and driven ends; for all three chambers the internal diameter is equal to 481 mm.

The firing mechanism is activated when the two scored steel diaphragms that separate the buffer chamber from the driver and driven chambers fail. The diaphragms' failure was obtained by a differential pressure created between the driver/buffer and buffer/driven chambers. During the failure of diaphragms four petals form and the rapid propagation of the pressurized gas into the driven chamber occurs leading to the creation of a shock wave.
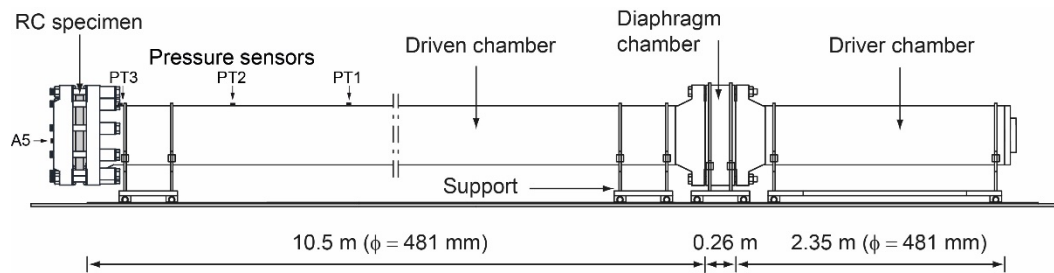
Figure 6 Schematic view of the shock tube

277   A picture of the test set-up area is shown in **Figure 7**. The equipment used to fix the specimen consists of two

278   steel crowns and a steel reaction flange (see **Figure 7a**). The specimens were placed between two steel crowns

279   specifically designed to guarantee a bilateral simply supported condition. The reaction end flange, consisting of a

280   slip-on flange of 20″, was connected to the driven-end flange using ten M52 bolts. An exploded view of the test

281   set-up area highlighting all the components is shown in **Figure 7a**, while an assembled view of the test set-up area

282   is shown in **Figure 7b-c**.
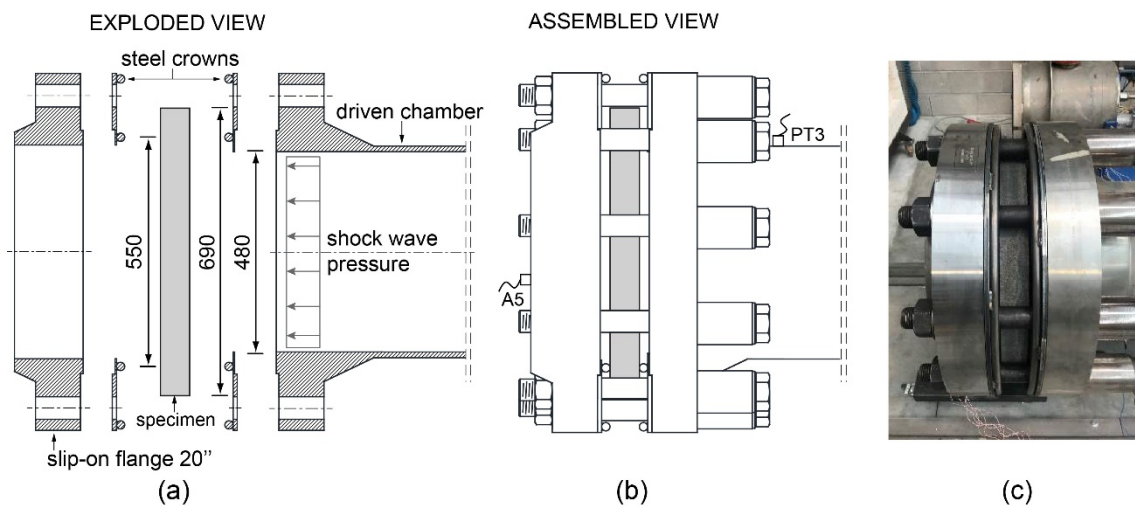
Figure 7 Details of the test set-up area: (a) exploded view, (b) assembled view and (c) picture in the assembled configuration

283   Mounting pressure sensors on a test sample to measure the load is not an easily practicable solution.

284   Nevertheless, if deformations in the concrete slabs are small, the data from the sensor closest to the specimen face

285   (sensor PT3) will provide a good approximation of the load that the concrete slabs experience.

286   **Table 3** summarizes the main properties that characterize the shock wave for each test: the peak pressure

287   (P_{peak}), the positive specific impulse (i_e^+) the duration of the positive specific impulse (t^+), and the shock wave

288   velocity (v_s). The latter was calculated using the data from sensors PT1-PT3. The pressure time histories for all

289   the blast tests recorded by the transducer closest to the specimen (sensor PT3 in **Figure 6**) are shown in **Figure 8**.

290   It is important to point out that the reflected pressure histories applied to the specimens are very repeatable. This

13

means that the change in stiffness of the specimens due to fire application does not lead to any significant contribution to the fluid-structure interaction phenomenon and therefore the mechanical problem can be considered uncoupled by shock wave propagation.

A problem occurred during test HP60 that prevented the correct recording of transducers PT1-PT3. Nevertheless, the high repeatability of these tests, clearly visible in **Figure 8**, allows the HP60 test results to be used as well.

Table 3 Shock wave characteristics

| Specimen ID	P_{peak}	i_e^+	t^+	v_s
	(kPa)	(kPa×ms)	(ms)	(m/s)
LP0	339.1	3430	33.2	502
LP60	393.6	3451	39.7	500
LP120	376.3	3278	29.2	502
HP0	1090	6255	17.5	652
HP60	-	-	-	-
HP120-1	1118	6288	17.7	674
HP120-2	1126	6181	16.9	714
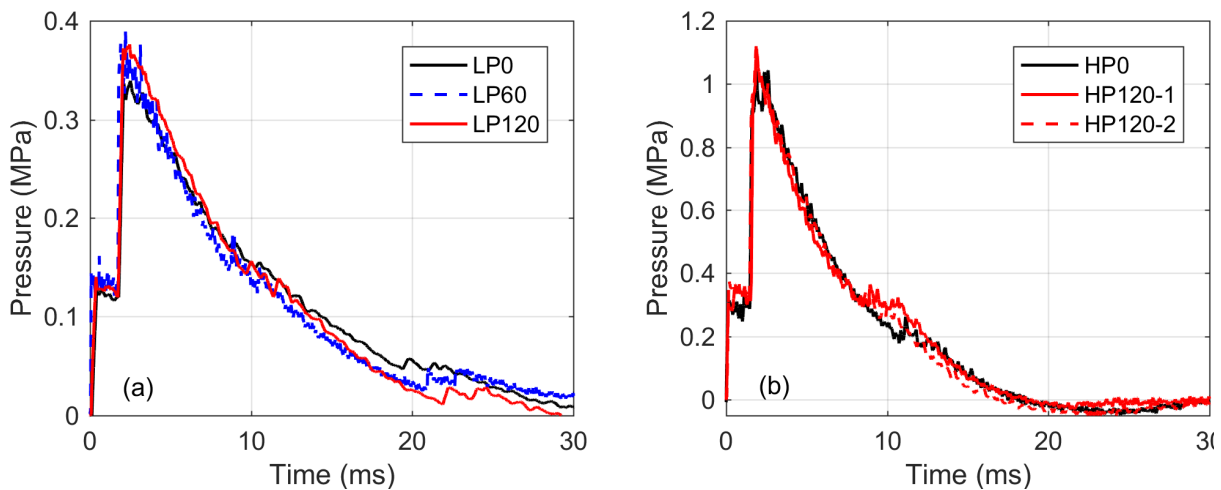
**Figure 8** Pressure–time histories for sensor PT3 in shock tube tests

4 TEST RESULTS

This section describes the main results obtained in the experimental investigation. **Figure 9** shows the evolution of temperatures, recorded by thermocouples T1-T4, as the fire exposure time varies. Clearly, the highest temperature is read by thermocouple T3 that is closest to the burner (see **Figure 4**). In specimens LP60 and HP60

303 (**Figure 9a-b**), exposed to high temperature for a time of 60 min, the maximum temperature reached is about 600

304 °C, while the temperature on the specimen side not exposed to the fire is about 250 °C. Looking at specimens

305 LP120 and HP120-1 (**Figure 9c-d**) both characterized by a fire exposure time of 120 min, the maximum

306 temperature reached is about 900 °C, while the temperature on the specimen side not exposed to the fire is about

307 450 °C. Although the fire curve was correctly applied to the HP60 specimen, a problem in data acquisition

308 occurred in this test after approximately 45 min of fire exposure (**Figure 9b**) and therefore the final data was lost.
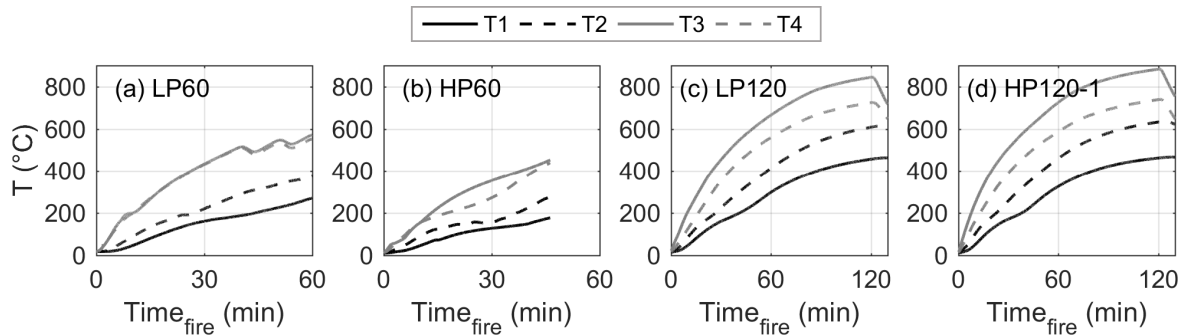
Figure 9 Evolution of temperatures vs fire exposure time: (a) test LP60, (b) test HP 60, (c) test LP120 and (d) HP120-1

309   The central accelerations of the specimens are compared in **Figure 10** for all the experimental tests. **Figure**

310 **10a** and **Figure 10b** compare low pressure (LP) and high pressure (HP) tests respectively, exposed to different

311 fire exposure times (0, 60, 120 min). The influence of fire exposure time on the acceleration response of the

312 specimens is illustrated and the elongation of the fundamental period of the specimens exposed to fire is clearly

313 visible compared to the specimens not subjected to fire exposure. While for LP tests the exposure to fire modifies

314 the frequency content of the response without significantly altering the maximum accelerations, in the HP tests

315 the exposure to fire involves both a modification of the frequency content and an increase in the amplitude of the

316 accelerations, thus indicating that the interaction between fire and blast is more pronounced.
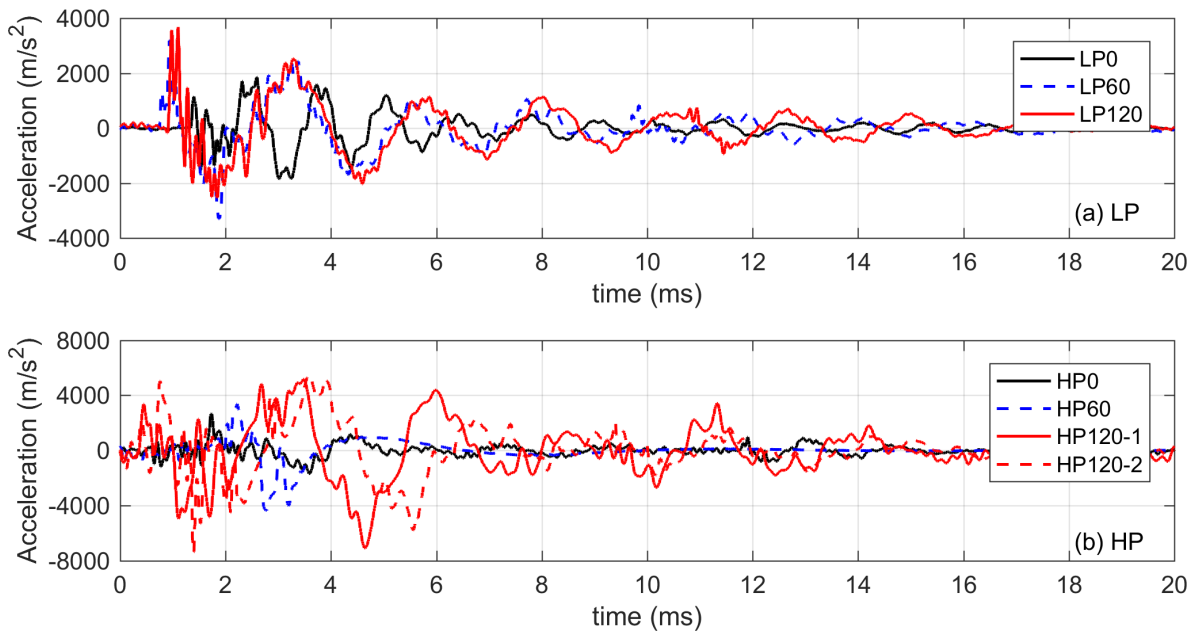
Figure 10 Axial central specimen accelerations A1: (a) tests LP0, LP60, LP120 and (b) tests HP0, HP60, HP120-1, HP120-2

317   When examining the frequency content of the recorded signals, it is important to remember that the shock tube

318   is deformable and not fixed to the ground but can be moved on a linear guide system. For this reason, the axial

319   acceleration of the tube was recorded during the tests using accelerometer A5 in order to distinguish the frequency

320   content of the shock tube from the frequency content associated with the response of the specimens. The shock

321   tube axial accelerations (A5) for tests HP0 and LP60, taken as an example, are shown in **Figure 11** together with

322   the corresponding frequency spectrum. The main frequency associated with the axial movement of the tube is

323   clearly visible in **Figure 11b** and is equal to about 100 Hz.
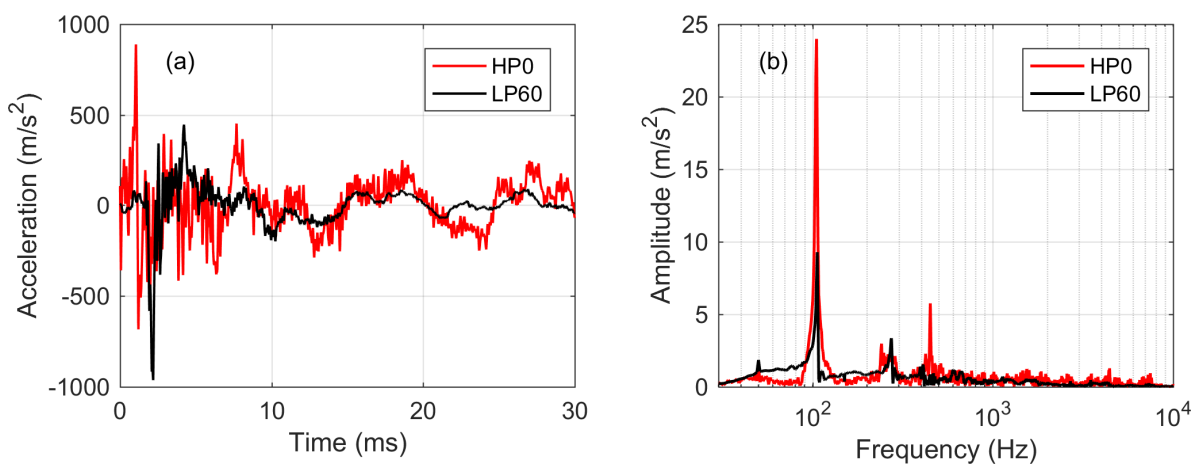
Figure 11 (a) Shock tube axial acceleration A5 for tests HP0 and LP60 and (b) corresponding frequency spectrum

324   **Figure 12** reports the results of the three accelerometers (A2–A4) placed at 120° in relation to each other on

325   the specimens. The specimens' responses are characterised by an elevated symmetry. While this result was to be

326   expected since the specimens are circular symmetric in terms of geometry and load, on the other hand the planarity

327   of the shock wave impacting the specimens is confirmed. It is also interesting to note that the symmetry in the

328   response is also preserved in the specimens exposed to the fire and which have therefore suffered damage (**Figure**

329   **12b-c-e-f**). In fact, the presence of spalling is limited to small regions and even where it affects the symmetry of

330   the specimen's geometry, it does not play a significant role on the symmetry of the specimens' response.

331
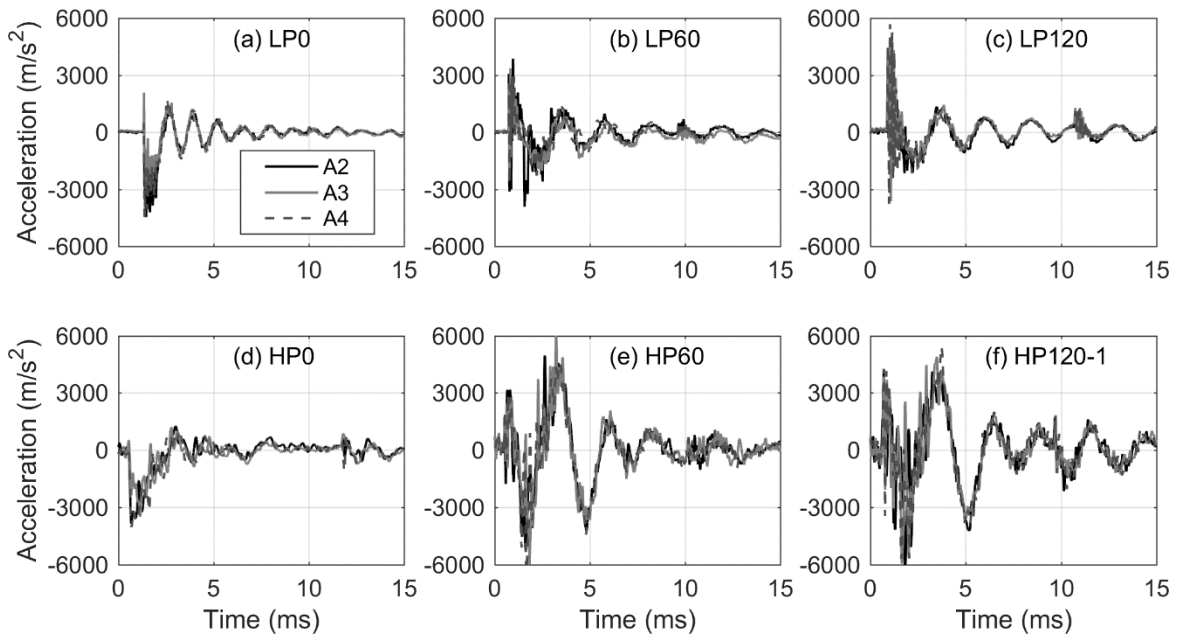
Figure 12 Axial specimen accelerations A2-A4: (a) test LP0, (b) test LP60, (c) test LP120, (d) test HP0, (e) test HP60 and (f) HP120-1

332   **Figure 13** shows front and rear crack patterns for all the tests with the exception of the LP0 test where no

333   cracks were detected at the end of blast test. Cracks that formed after the fire exposure are depicted in red, whilst

334   cracks that formed after the blast test are depicted in black. The LP0 test in which the blast load was applied

335   without a high temperature exposure was characterized by the absence of cracks indicating as planned a linear

336   elastic behaviour of the specimen. Looking at the HP0 specimen, characterized by a higher peak pressure and a

337   higher impulse than specimen LP0 without fire exposure, a slight crack pattern both on the rear and front faces

338   can be noted. Fire exposure induces quite severe damage in the specimens, revealed by the crack patterns shown

339   in **Figure 13a-b-d-e-f**. On the front face, the area in contact with the flame is clearly identifiable having a different

340   colour and slight concrete spalling is visible in all the specimens exposed to fire (see grey regions in **Figure 13a-**

b-d-e-f). **Figure 14** shows the exposed surface of LP60 and HP120-2 specimens after the fire tests, as an example of each exposure time. In the pictures, both the area in contact with the flame and the region of concrete spalling can be easily recognized.
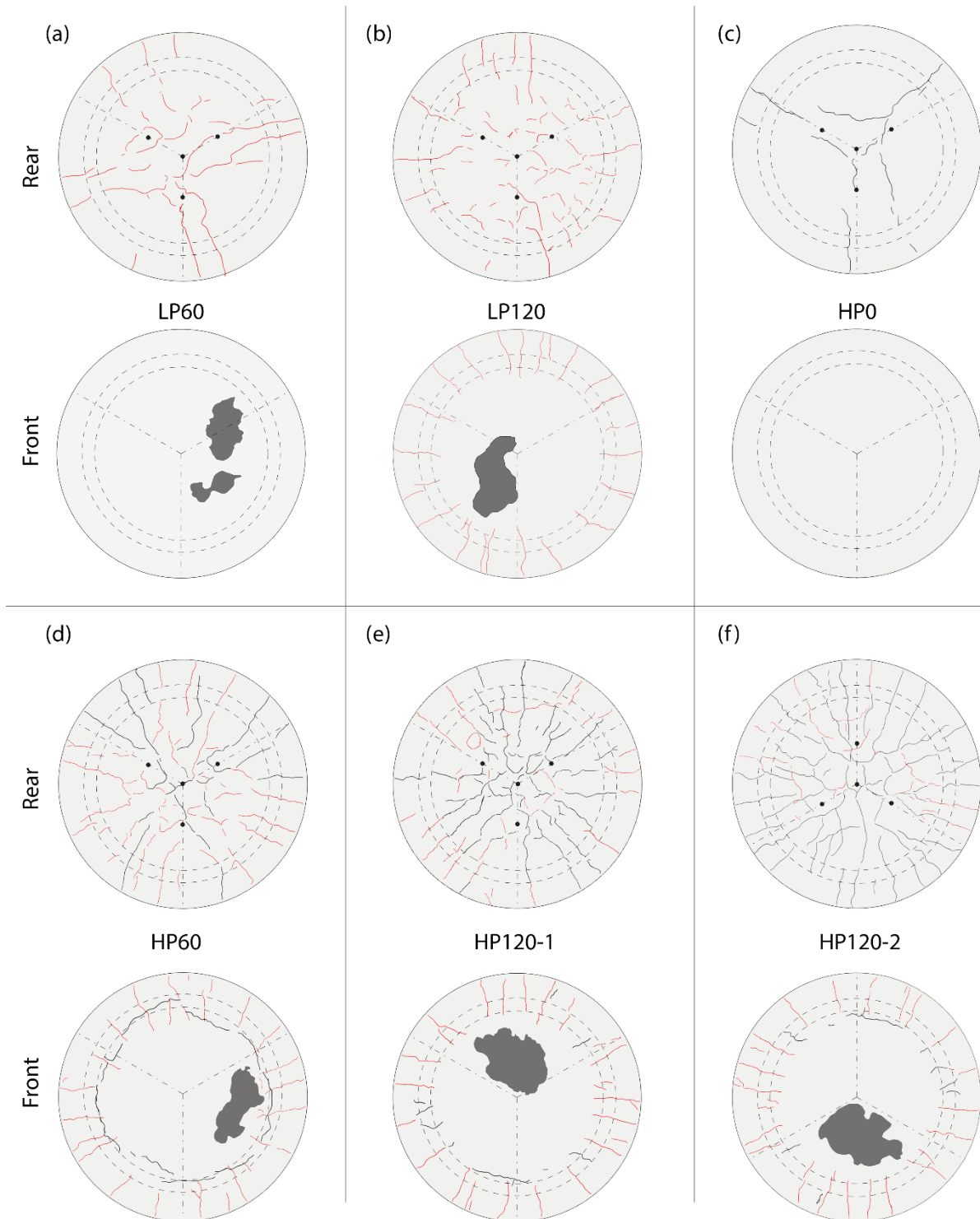

Figure 13 Front and rear crack patterns for tests (a) LP60, (b) LP120, (c) HP0, (d) HP60, (e) HP120-1 and (f) HP120-2. Thermal and pressure cracks are indicated in red and in black respectively.

344 Radial cracks are always visible in all specimens exposed to fire. The radial cracks on the outer ring region of

345 the slabs are mainly caused by the heating process that is directly applied to the central core of the slab. The

346 thermal gradient between the central core and the external ring, because of the compatibility of the two regions,

347 cause a circumferential tensile state of stress in the outer ring leading to the radial crack formation. In the

348 specimens tested in HP conditions after fire exposure it is also possible to observe some circumferential cracks

349 on the loaded surface (especially visible for HP60, **Figure 13d**). This is due to the fact that, because the fire is

350 applied only to the central region, the initial damage of the structure is not uniform along the radius but is more

351 concentrated in the central heated region thus also creating a variation of the local sectional stiffness along the

352 radius. The presence of an outer stiffer region affects the boundary condition thus also leading to the formation of

353 radial tensile stresses on the loaded surface. In the case of a fire exposure time of 120 min, these cracks are less

354 pronounced because the longer fire exposure leads to a more uniform distribution of the temperature and

355 subsequently more uniform damage even along the radius.

356 The application of a blast load after the fire exposure has limited effects for specimens LP60 and LP120 since

357 no new cracks were detected after the exposure to fire (**Figure 13a-b**). A different trend can be observed in **Figure**

358 **13d-e-f** for HP tests where the application of a blast load after the fire exposure produces further cracks in the

359 specimens. It can be concluded that in LP tests, the main source of damage is the fire, while in HP tests both fire

360 and blast contribute to the damage of the specimens, and the effect of blast is more amplified when a more severe

361 fire exposure is applied.

362
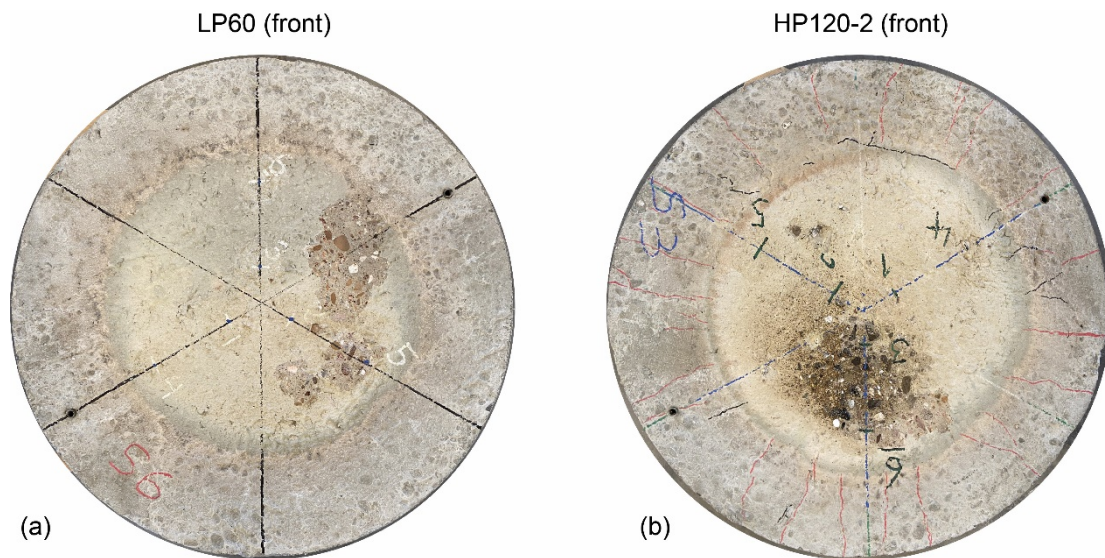
Figure 14 Furnace flame footprint and spalling area for tests (a) LP60 and (b) HP120-2.

363   Direct UPV measurements were carried out on the specimens before and after fire and blast loads. The aim of

364   these measurements was to establish if, in case of fire and blast, the wave velocity decreases compared to the

365   velocity in the pristine specimen, thus indicating that internal damage occurred in the specimen. Six points were

366   monitored (**Figure 3**) and average wave velocities are considered in the following discussion. **Figure 15** reports

367   the average percentage reduction of wave velocity induced by fire and blast compared to the initial undamaged

368   situation. In **Figure 15a,** LP tests are examined first: effects of fire exposure are clearly visible leading to a wave

369   velocity reduction of about 40% and 55% for fire exposure of 60 min and 120 min, respectively. In LP tests, the

370   application of the blast load after the fire exposure does not significantly change the wave velocity, in line with

371   the observed crack patterns discussed above. Looking at the HP tests, the wave velocity reduction due to fire

372   exposure only is similar to that of LP tests. The application of a blast load in specimens already damaged by fire

373   leads to a further reduction of the wave's velocity highlighting an increase in damage especially in specimens

374   subjected to a fire exposure of 120 min. It should be emphasized that the cracks through the thickness of the

375   specimen are not fully visible with direct UPV measurements. This justifies crack patterns on the specimens that

376   are more severe than suggested by measurements with direct UPV.
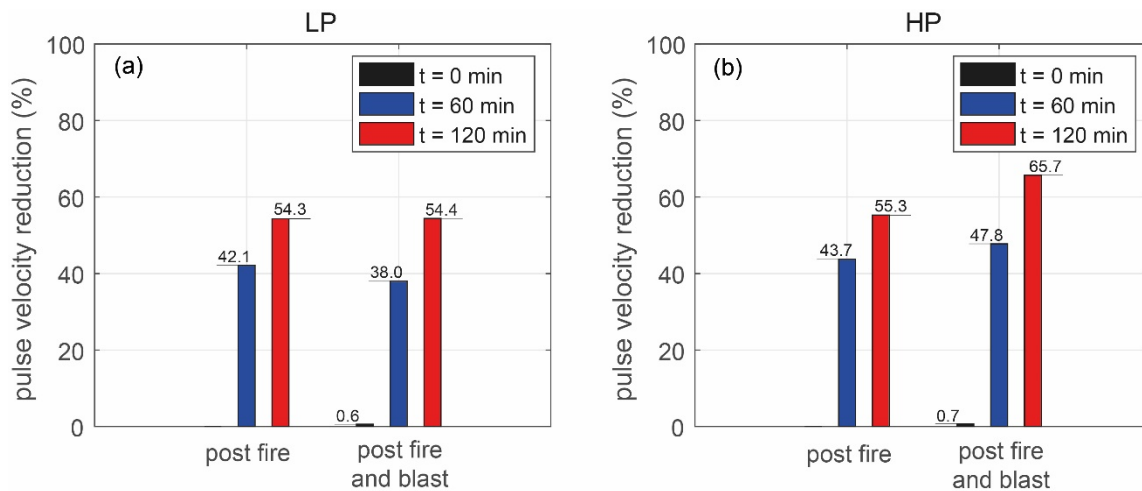
Figure 15 Percentage reduction of direct ultrasonic pulse velocity results induced by fire and blast: (a) LP tests
and (b) HP tests

5   DISCUSSION

378   The experimental results presented in Section 4 are further analysed in this section using simplified tools,

379   specifically: (i) an equivalent elastic single degree of freedom (SDOF) model and (ii) a linear elastic finite element

380   (FE) model. Despite their simplicity, methods (i) and (ii) can be a useful tool to provide a deeper insight into the

381   experimental results.

382   With reference to the equivalent SDOF model, the mass, the stiffness and the applied load of the RC slabs are

383   replaced in the equation of motion with the equivalent values of a lumped mass–spring system. The principle of

384   virtual displacement makes it possible to find the transformation coefficients that relate the equivalent mass,

385   stiffness and load in the SDOF system to their respective quantities in the actual slabs. The equivalent system has

386   kinetic energy, strain energy and external work equal to the distributed system [48]. In calculating the

387   transformation factors necessary to develop the equivalent SDOF model, a simplification was adopted: the loading

388   area is extended up to the radius $r_1 = 275$ mm equal to the position of the support (see **Figure 7a**). The equivalent

389   system has a total diameter equal to the real specimen slab ($r_2 = 345$ mm). The elastic transformation factors

390   used in this study are similar to those given in [49] for a simply supported plate; the exception is represented by

391   the slab radius r_2 that does not coincide with the support radius r_1. The material parameters necessary to describe

392   the SDOF model are the average values reported in Section 2.1.

393   With reference to the linear elastic FE model, this was built and processed in the Abaqus 6.14-5 environment

394   [50], and consists of 7987 3-node triangular shell elements (element S3, average edge size 10 mm) connected

395   through 4103 nodes. Boundary conditions and the blast load are applied according to the experimental set-up

396   shown in **Figure 7**. The elastic modulus of the concrete measured experimentally ($E \cong 28000$ MPa) was

397   corrected by a factor of 1.15 to take into account the stiffening effect of the reinforcement following an

398   homogenized approach for RC sections. The Young's modulus E, the Poisson's ratio ν and the density ρ adopted

399   in the FE model are then assumed to be equal to $E = 32000$ MPa, $\nu = 0.2$ and $\rho = 2500$ kg/m^3. The finite element

400   model, due to its simplicity, was used mainly for eigenfrequency analysis and for studying the dynamic response

401   of the specimen that under blast loads did not show any damage (i.e. LP0). In this regard, specimen LP0 is an

402   important reference to better understand the structural behaviour of all the other specimens.

403   **Figure 16a** compares the central slab acceleration A1 recorded during the reference test LP0 with those

404   obtained with the equivalent elastic SDOF model and with the FE model. The experimental acceleration is well

405   reproduced by both simplified models. The frequency spectrum of the experimental signal A1 is compared with

406   the numerical one (i.e. FE) in figure **Figure 16b**. The first numerical frequency ($f_{1,num} = 780$ Hz) is almost

407   identical to the experimental one ($f_{1,exp} = 787$ Hz); the second and third experimental peaks visible in **Figure**

408   **16b** are overestimated by the FE model that results to be stiffer than the real slab. The SDOF model provides a

409   first natural frequency equal to $f_{1,SDOF} = 812$ Hz that is slightly higher than the experimental one, but it can be

410   considered a satisfactory prediction.

411   The experimental peak visible at the lowest frequency of about 100 Hz is not related to the slab response, but

412   it depends on the shock tube's axial movement and should not be considered in the following discussion (see
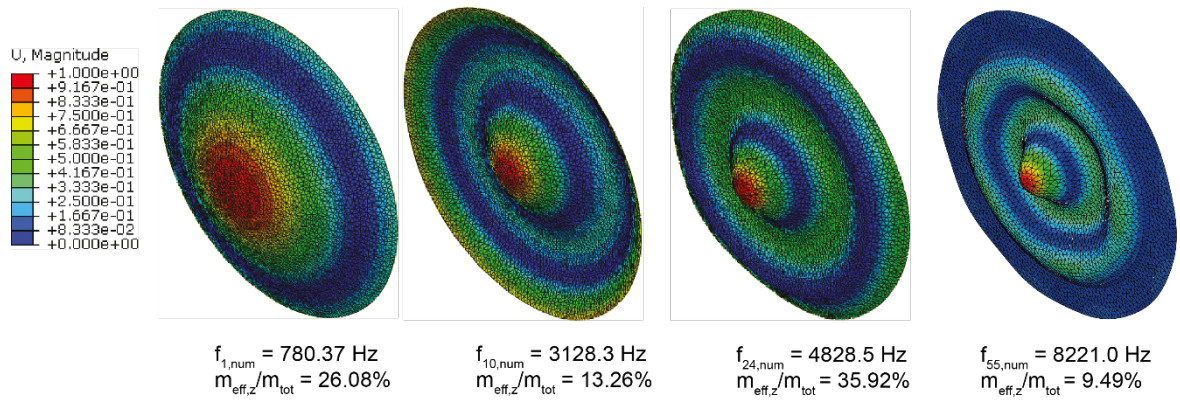
413   Section 4).
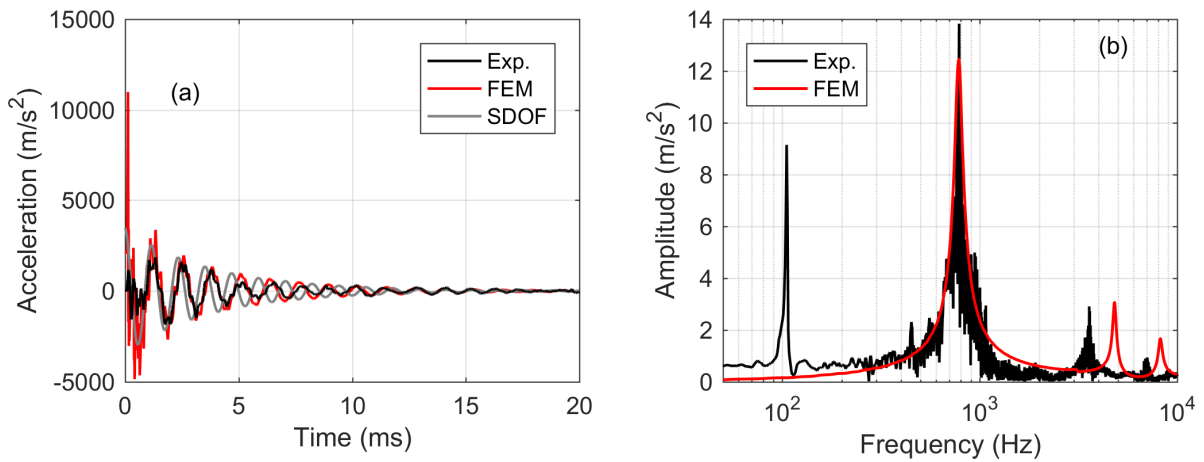
Figure 16 Test LP0: a) time history acceleration A1 and b) frequency spectrum of signal A1

414   **Figure 17** illustrates the first four significant mode shapes of the FE model (Modes 1, 10, 24 and 55). These

415   four mode shapes involve an out-of-plane translation (the z direction) with an activation of the effective mass

416   involved in z direction normalized with respect to the total mass of the model of 26%, 13%, 36 % and 9%

417   respectively. Mode shapes not shown in **Figure 17** involve negligible effective mass.
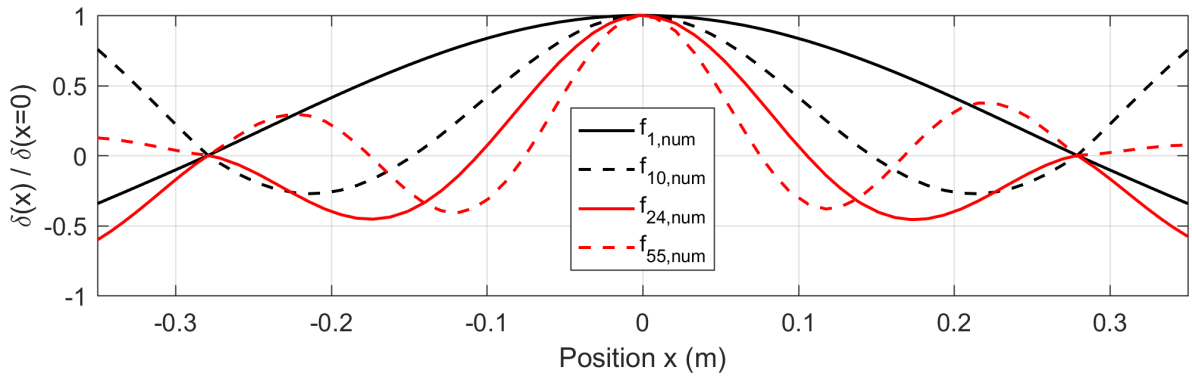
418   Given the good prediction of the slab's central acceleration provided by the SDOF system, it could be stated

419   that the first mode of vibration mainly governs the slab's response. For this reason, a detailed analysis of this

420   mode is discussed in the following.

421   By examining the frequency content of the signal A1 of all the specimens recorded during the blast tests it is

422   also possible to establish the variation of the fundamental frequency $f_{1,exp}$ as the fire exposure time varies (**Figure**

423   **18**). The variation of the fundamental frequency is directly correlated to the variation (reduction) of the stiffness

424   of the specimen and is ultimately a measure of the accumulated damage. Looking at the LP tests and keeping in

425   mind that test LP0 corresponds to an undamaged state, the fire exposure reduced the fundamental frequency by

426   50% providing a first frequency equal to about 400 Hz for a fire exposure time of both 60 and 120 min. Observing

427   the HP tests, there is a reduction of the first frequency of 25% compared to the non-damaged situation for the blast

428   effect only (test HP0). The exposure to fire further reduces the first frequency to values below 400 Hz for the

429   HP120 tests, that corresponds to a first frequency reduction higher than 50% compared to the pristine specimen.

f_{1,num} = 780.37 Hz
m_{eff,z}/m_{tot} = 26.08%

f_{10,num} = 3128.3 Hz
m_{eff,z}/m_{tot} = 13.26%

f_{24,num} = 4828.5 Hz
m_{eff,z}/m_{tot} = 35.92%

f_{55,num} = 8221.0 Hz
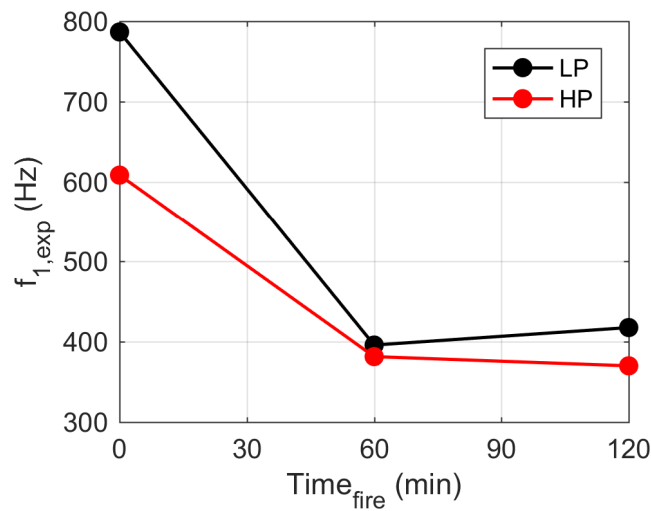m_{eff,z}/m_{tot} = 9.49%

(a)

(b)

Figure 17 First, tenth, twenty-fourth and fifty-fifth numerical modal shapes: (a) 3D views and (b) normalized displacement profiles along one diameter (U: normalized displacement amplitude)

430

Figure 18 Variation of the first experimental frequency $f_{1,exp}$ with the variation of the fire exposure time for the LP and HP tests

431   A Frequency Domain Decomposition (FDD) approach [51] was adopted to define the experimental modes of

23

432   vibration of the slabs starting from the measurements of the accelerations during the tests. **Figure 19a** compares

433   the mode shape of the first mode of vibration provided by the eigenfrequency analysis with the mode shape

434   obtained by the application of an FDD procedure to the experimental accelerations measured for test LP0. The

435   figure represents the deformed shape of a diameter of the specimen considering a reference system placed in the

436   centre of the slab (x=0). Due to the small amount of accelerometers placed on the specimens, just the dotted points

437   at x = 0 and x = ± 0.12 m can be experimentally obtained, while the zero displacement condition is imposed at the

438   support (x = ± 0.275 m). The figure shows good agreement between the experimental deformed shape and the

439   numerical prediction; this comparison proves that the boundary conditions applied in the tests represent a simply

440   supported condition well.

441   **Figure 19b** presents the mode shape of the first mode of vibration for the different tests performed. The

442   deformed shape of the first mode is almost identical for all the LP tests and for the HP0 test, while a slight

443   difference can be observed for the two HP120 tests. The damage induced by both fire and blast seems to have a

444   limited effect on the first mode shape despite the change in mode frequency.

445
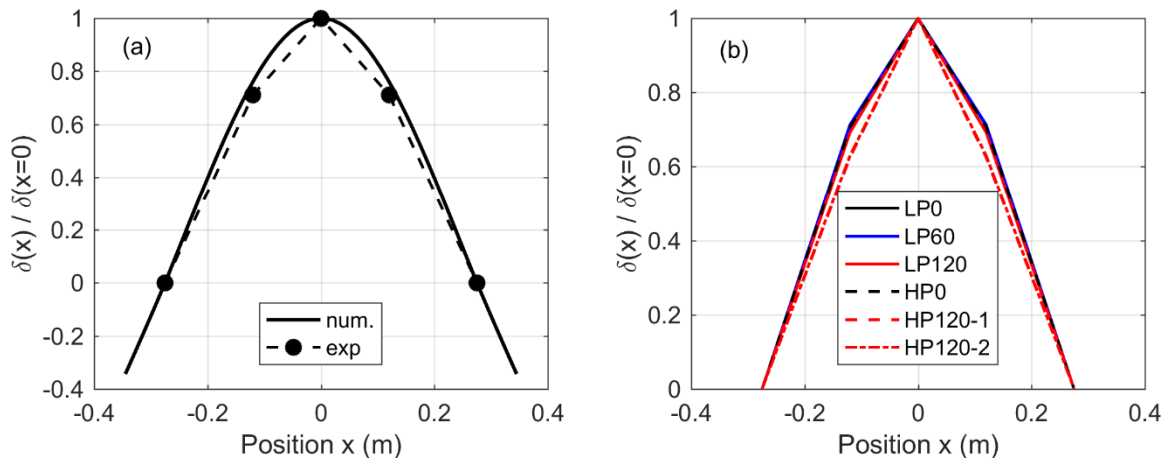
Figure 19 (a) comparison between experimental (LP0) and numerical first modal shape; (b) first modal shape derived from experimental data for all the specimens

446   Damping is generally considered as a reliable indicator of damage in structures [52] and several studies have

447   pointed out the effect of damage on damping [53][54][55][56][57]. Other investigations have even shown how

448   cracks in RC structures could induce an increase of damping ratio [58] and that the change in damping is well

449   correlated even to the crack depth [59].

450   The analysis of the decay of the acceleration peaks for all the experimental tests makes it possible to estimate

451   the damping ratio ζ_{exp} and its variation compared to the undamaged situation (**Figure 20**). Using the acceleration

452   record ($\ddot{u}$) of the free vibration phase, the damping ratio was determined from:

$$\zeta_{exp} = \frac{1}{2\pi j} \ln \frac{\ddot{u}_i}{\ddot{u}_{i+j}} \tag{1}$$

453   where $\ddot{u}_i$ is the acceleration at the peak i and $\ddot{u}_{i+j}$ the acceleration at the peak $i+j$. Eq. (1) is valid for a lightly

454   damped system. The damping ratio defined in Eq. (1) is a linear feature of damping and represents the extent of

455   energy dissipation in the samples [52]. The presence of fire damage and/or cracks leads to larger energy dissipation

456   and therefore to a larger damping ratio.
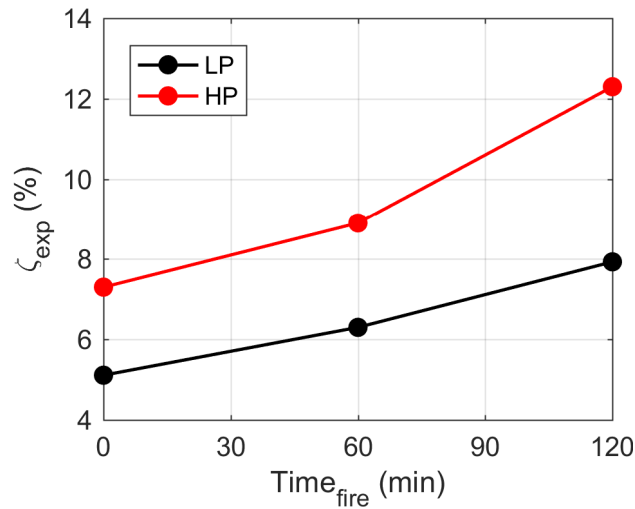
Figure 20 Variation of damping ratio ζ_{exp} with the variation of the fire exposure time for the LP and HP tests

457   While the damping was approximately 5% for the LP0 specimen, the 60 min fire exposure (test LP60)

458   increases the damping to 6%, and the 120 min fire exposure (LP120) further increases it to 7%. Looking at the

459   HP tests, applying a higher peak pressure and impulse than the LP tests results in an increase of damping ratio

460   equal to 7%. The combined effect of blast and fire leads to an increase in damping ratios of 9% and 12% for fire

461   exposure times of 60 and 120 min, respectively. While the black curve in **Figure 20** can be seen as the exclusive

462   contribution of the fire, the red curve represents the combined effect of blast and fire.

463   An ad-hoc subroutine was developed in a LabVIEW environment to derive reliable displacement

464   measurements from the central acceleration signals A1 (**Figure 21**). This subroutine consists of a double time

465   integration of the acceleration applying a low pass filter at a frequency of 80 kHz before each time integration

466   step.

467   The effect of damage due to exposure to fire compared to the pristine specimen is clearly visible for both the

468   LP (**Figure 21a**) and HP (**Figure 21b**) tests. In both figures the period elongation due to the combined effects of

469   blast and fire is visible. For HP tests, the period elongation is also combined with an amplification of the maximum

displacements with peaks that can be 3 times higher for specimens subjected to a fire exposure of 120 min compared to specimens without fire exposure.
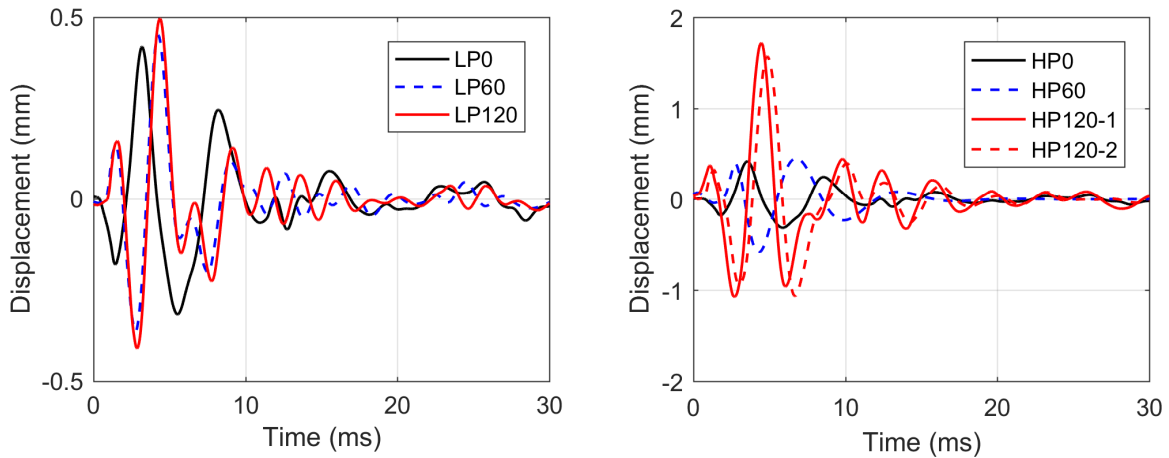
Figure 21 Displacement time history responses derived using a LabVIEW subroutine for (a) LP tests and (b) HP tests

6   CONCLUDING REMARKS

In this study, the structural performance of reinforced concrete (RC) slabs subjected to combined fire and blast actions were investigated experimentally. The sequence of fire and blast was obtained using proper gas burner equipment and a shock tube device. Simplified numerical tools, namely (i) an equivalent elastic single degree of freedom (SDOF) model and (ii) a linear elastic finite element (FE) model were also used to provide a deeper insight into the experimental results. Based on this research, the following conclusions can be drawn:

- The shock tube used in the blast tests produced consistent and blast-like loading conditions characterized by high repeatability. Accelerometer recordings placed at 120° on the specimens confirm the planarity of the shock wave impacting the specimens.

- Test results pointed out the negligible role of the fluid-structure interaction in the cases investigated even when the samples were previously exposed to fire curves.

- Temperature evolutions, monitored using thermocouples embedded through the thickness of the slabs, show that the slabs reach temperatures between $250 - 600°C$ and between $450 - 900°C$ for fire exposure times of 60 and 120 min, respectively.

- Fire exposure causes cracks on both faces of the specimen; some of these cracks pass through the thickness. Limited concrete spalling was observed when the fire exposure was equal to 120 min. In LP tests, the subsequent application of blast loads after fire exposure does not significantly change the crack pattern. On the contrary, in HP tests the higher peak pressure and the higher impulse compared to LP tests induce new

cracks in the specimens. This effect is maximized when the fire exposure time is higher (120 min).

- Fire exposure induces a pronounced decrease of strength and stiffness in the specimens, as pointed out by the analysis of (i) the crack patterns, (ii) the first frequency shift and (iii) the reduction of the wave velocity recorded using UPV measurements.

- The analysis of the frequency spectrum of the accelerometer signals shows a significant reduction of the slab's first frequency that was higher than 50% for HP120 tests compared to the pristine specimen.

- Experimental data makes it possible to estimate the evolution of the damping ratio as the fire exposure time varies and for different blast pressure levels. The damping ratios range between 5% for pristine specimen to 12% for HP120 tests, thus providing an indication of the damage accumulated by the slab specimens.

- The eigenvalue analysis on a simplified FE shell model provides a first numerical frequency that is in good agreement with the experimental one. This confirms the correctness of the set-up used during the shock tube tests that can be schematized as a simply supported condition. The simplified SDOF model also provides a fundamental frequency in good agreement with the experimental data.

- An ad-hoc subroutine developed in a LabVIEW environment made it possible to derive displacement estimations from the acceleration signals. The analysis of the specimens' central displacement shows that a greater exposure time to fire corresponds to greater displacement peaks in response to the blast loads. The maximum displacement values were 3 times higher for specimens subjected to a fire exposure of 120 min compared to specimens without fire exposure.

- The experimental data presented in this work is valuable in order to define a reliable benchmark for numerical models which, upon numerical upscaling, will be instrumental for the design of tunnels under exceptional load conditions, such as the combined action of fire and subsequent internal explosion.

REFERENCES

[1] Beard A, Carvel R. Handbook of Tunnel Fire Safety. second edi. ICE Publishing; 2012.

[2] Kodur V, Naser M. Structural Fire Engineering. McGraw-Hill; 2020.

[3] Savov K, Lackner R, Mang HA. Stability assessment of shallow tunnels subjected to fire load. Fire Saf J 2005;40:745–63. doi:10.1016/j.firesaf.2005.07.004.

[4] Pichler C, Lackner R, Mang HA. Safety Assessment of Concrete Tunnel Linings under Fire Load. J Struct

521   Eng 2006;132:961–9. doi:10.1061/(asce)0733-9445(2006)132:6(961).

522   [5]   Yan ZG, Zhu HH, Woody Ju J, Ding WQ. Full-scale fire tests of RC metro shield TBM tunnel linings.
523   Constr Build Mater 2012;36:484–94. doi:10.1016/j.conbuildmat.2012.06.006.

524   [6]   Lilliu G, Meda A. Nonlinear phased analysis of reinforced concrete tunnels under fire exposure. J Struct
525   Fire Eng 2013;4:131–42. doi:10.1260/2040-2317.4.3.131.

526   [7]   Felicetti R. Assessment Methods of Fire Damages in Concrete Tunnel Linings. Fire Technol
527   2013;49:509–29. doi:10.1007/s10694-011-0229-6.

528   [8]   Wang F, Wang M, Huo J. The effects of the passive fire protection layer on the behavior of concrete
529   tunnel linings: A field fire testing study. Tunn Undergr Sp Technol 2017;69:162–70.
530   doi:10.1016/j.tust.2017.06.021.

531   [9]   Sakkas K, Vagiokas N, Tsiamouras K, Mandalozis D, Benardos A, Nomikos P. In-situ fire test to assess
532   tunnel lining fire resistance. Tunn Undergr Sp Technol 2019;85:368–74. doi:10.1016/j.tust.2019.01.002.

533   [10]   Sun Z, Zhang Y, Yuan Y, Mang HA. Stability analysis of a fire-loaded shallow tunnel by means of a
534   thermo-hydro-chemo-mechanical model and discontinuity layout optimization. Int J Numer Anal
535   Methods Geomech 2019;43:2551–64. doi:10.1002/nag.2991.

536   [11]   Lo Monte F, Felicetti R, Meda A, Bortolussi A. Explosive spalling in reinforced concrete tunnels exposed
537   to fire: Experimental assessment and numerical modelling. In: Peila D, Viggiani G, Viggiani G, Celestino
538   T, editors. Tunnels Undergr. Cities Eng. Innov. meet Archaeol. Archit. Art- Proc. WTC 2019 ITA-AITES
539   World Tunn. Congr., CRC Press/Balkema; 2019, p. 2519–26.

540   [12]   Agrawal A, Kodur VKR. A Novel Experimental Approach for Evaluating Residual Capacity of Fire
541   Damaged Concrete Members. Fire Technol 2020;56:715–35. doi:10.1007/s10694-019-00900-1.

542   [13]   Stucchi R, Amberg F. A Practical Approach for Tunnel Fire Verification. Struct Eng Int 2020:1–15.
543   doi:10.1080/10168664.2020.1772697.

544   [14]   EN 1991-1-2. Eurocode 1: Actions on structures—Part 1–2: General actions—Actions on structures
545   exposed to fire. Brussels: 2004.

546   [15]   EN 1992-1-2. Eurocode 2: Design of concrete structures— Part 1–2: General rules—Structural fire design.
547   Brussel: 2004.

548   [16]   Feldgun VR, Kochetkov A V., Karinski YS, Yankelevsky DZ. Internal blast loading in a buried lined
549   tunnel. Int J Impact Eng 2008;35:172–83. doi:10.1016/j.ijimpeng.2007.01.001.

550   [17]   Liu H. Dynamic analysis of subway structures under blast loading. Geotech Geol Eng 2009;27:699–711.
551   doi:10.1007/s10706-009-9269-9.

552   [18]   Liu H. Soil-Structure Interaction and Failure of Cast-Iron Subway Tunnels Subjected to Medium Internal
553   Blast Loading. J Perform Constr Facil 2012;26:691–701. doi:10.1061/(asce)cf.1943-5509.0000292.

554   [19]   Colombo M, Martinelli P, di Prisco M. Underground tunnels exposed to internal blast: Effect of the
555   explosive source position. vol. 711. 2016. doi:10.4028/www.scientific.net/KEM.711.852.

556   [20]   Gao M, Zhang JY, Chen QS, Gao GY, Yang J, Li DY. An exact solution for three-dimensional (3D)
557   dynamic response of a cylindrical lined tunnel in saturated soil to an internal blast load. Soil Dyn Earthq
558   Eng 2016;90:32–7. doi:10.1016/j.soildyn.2016.08.031.

559   [21]   Yu H, Wang Z, Yuan Y, Li W. Numerical analysis of internal blast effects on underground tunnel in soils.
560   Struct Infrastruct Eng 2016;12:1090–105. doi:10.1080/15732479.2015.1077260.

561 [22] Zhao Y, Chu C, Vafeidis A, Li J. Vibration of a Cylindrical Tunnel under a Centric Point-Source
562   Explosion. Shock Vib 2017;2017. doi:10.1155/2017/9152632.

563 [23] Kristoffersen M, Minoretti A, Børvik T. On the internal blast loading of submerged floating tunnels in
564   concrete with circular and rectangular cross-sections. Eng Fail Anal 2019;103:462–80.
565   doi:10.1016/j.engfailanal.2019.04.074.

566 [24] Prasanna R, Boominathan A. Finite-Element Studies on Factors Influencing the Response of Underground
567   Tunnels Subjected to Internal Explosion. Int J Geomech 2020;20:04020089. doi:10.1061/(asce)gm.1943-
568   5622.0001678.

569 [25] Goel MD, Verma S, Panchal S. Effect of Internal Blast on Tunnel Lining and Surrounding Soil. Indian
570   Geotech J 2020. doi:10.1007/s40098-020-00451-1.

571 [26] Minoretti A, Xiang X, Johansen IL, Eidem M. The Future of the Tunnel Crossing: The Submerged
572   Floating Tube Bridge. Struct Eng Int 2020:1–5. doi:10.1080/10168664.2020.1775165.

573 [27] Kakogiannis D, Pascualena F, Reymen B, Pyl L, Ndambi JM, Segers E, et al. Blast performance of
574   reinforced concrete hollow core slabs in combination with fire: Numerical and experimental assessment.
575   Fire Saf J 2013;57:69–82. doi:10.1016/j.firesaf.2012.10.027.

576 [28] Pascualena F, Ndambi J, Reymen B, Desmet B, Segers E, Vantomme J. Blast performance of concrete
577   slabs in combination with fire. Proc. 8th Int. Conf. Struct. Dyn. EURODYN 2011, Leuven; Belgium:
578   2011, p. 3310–7.

579 [29] Ruan Z, Chen L, Fang Q. Numerical investigation into dynamic responses of RC columns subjected for
580   fire and blast. J Loss Prev Process Ind 2015;34:10–21. doi:10.1016/j.jlp.2015.01.009.

581 [30] Zhai C, Chen L, Xiang H, Fang Q. Experimental and numerical investigation into RC beams subjected to
582   blast after exposure to fire. Int J Impact Eng 2016;97:29–45. doi:10.1016/j.ijimpeng.2016.06.004.

583 [31] Zhang Q, Wang WY, Bai SS, Tan YH. Response analysis of tunnel lining structure under impact and fire
584   loading. Adv Mech Eng 2019;11:1–6. doi:10.1177/1687814019834473.

585 [32] Colombo M, Martinelli P, di Prisco M. A design approach for tunnels exposed to blast and fire. Struct
586   Concr 2015;16. doi:10.1002/suco.201400052.

587 [33] Colombo M, di Prisco M, Martinelli P. A New Shock Tube Facility for Tunnel Safety. Exp Mech 2011;51.
588   doi:10.1007/s11340-010-9430-7.

589 [34] Arano A, Colombo M, Martinelli P, Øverli JA, Hendriks MA, Kanstad T, et al. Material Characterization
590   Approach for Modelling High-Strength Concrete after Cooling from Elevated Temperatures. J Mater Civ
591   Eng 2020. doi:10.1061/(ASCE)MT.1943-5533.0003694.

592 [35] ITA-AITES. Guidelines for Structural Fire Resistance for Road Tunnels. 2004.

593 [36] ISO 1920-10:2010. Testing of concrete - Part 10: Determination of static modulus of elasticity in
594   compression. 2010.

595 [37] ISO 15630-1:2019. Steel for the reinforcement and prestressing of concrete - Test methods - Part 1:
596   Reinforcing bars, rods and wire. 2019.

597 [38] Timoshenko S, Woinowsky-Krieger S. Theory of plates and shells. New York: McGraw-Hill; 1959.

598 [39] Johansen K. Yield-line theory. London: Cement and Concrete Association; 1962.

599 [40] Bungey J, Millard S, Grantham M. Testing of Concrete in Structures. 4th editio. London: Taylor and
600   Francis; 2006. doi:https://doi.org/10.1201/9781482264685.

601 [41] Ritzel D, Thibault P. Development of an efficient low-cost blast tube facility. Tenth Int. Symp. Mil. Appl.
602   Blast Simul. (MABS 10), Freiburg, Germany: 1987.

603 [42] NATO-AEP-25. Nuclear Blast and Thermal Test Methods and Procedures. NATO Allied Engineering
604   Publication; 1995.

605 [43] Toutlemonde F, Rossi P, Boulay C, Gourraud C, Guedon D. Dynamic behaviour of concrete: tests of slabs
606   with a shock tube. Mater Struct 1995;28:293–8. doi:10.1007/BF02473264.

607 [44] Kristoffersen M, Pettersen JE, Aune V, Børvik T. Experimental and numerical studies on the structural
608   response of normal strength concrete slabs subjected to blast loading. Eng Struct 2018;174:242–55.
609   doi:10.1016/j.engstruct.2018.07.022.

610 [45] Colombo M, Martinelli P, di Prisco M. Layered high-performance concrete plates interacting with
611   granular soil under blast loads: An experimental investigation. Eur J Environ Civ Eng 2013;17.
612   doi:10.1080/19648189.2013.841595.

613 [46] Colombo M, Martinelli P, di Prisco M. On the blast resistance of high performance tunnel segments.
614   Mater Struct Constr 2016;49. doi:10.1617/s11527-014-0480-7.

615 [47] Andreotti R, Colombo M, Guardone A, Martinelli P, Riganti G, Di Prisco M. Performance of a shock tube
616   facility   for   impact   response   of   structures.   Int   J   Non   Linear   Mech   2015;72.
617   doi:10.1016/j.ijnonlinmec.2015.02.010.

618 [48] Biggs J. Introduction to structural dynamics. New York: McGraw-Hill; 1964.

619 [49] Colombo M, Martinelli P. Pressure-impulse diagrams for RC and FRC circular plates under blast loads.
620   Eur J Environ Civ Eng 2012;16. doi:10.1080/19648189.2012.675149.

621 [50] Dassault Systèmes. Abaqus Analysis User's Manual - Version 6.14 2016.

622 [51] Brincker R, Zhang L, Andersen P. Modal identification from ambient responses using frequency domain
623   decomposition. Proc. Int. Modal Anal. Conf. - IMAC, 2000, p. 625–30.

624 [52] Cao MS, Sha GG, Gao YF, Ostachowicz W. Structural damage identification using damping: A
625   compendium of uses and features. Smart Mater Struct 2017;26. doi:10.1088/1361-665X/aa550a.

626 endStates) 1990;116:1660–78.

627 [54] Rezaee M, Hassannejad R. Free vibration analysis of simply supported beam with breathing crack using
628   perturbation method. Acta Mech Solida Sin 2010;23:459–70. doi:10.1016/S0894-9166(10)60048-1.

629 [55] Chandra R, Singh SP, Gupta K. A study of damping in fiber-reinforced composites. J Sound Vib
630   2003;262:475–96. doi:10.1016/S0022-460X(03)00107-X.

631 [56] Kyriazoglou C, Guild FJ. Quantifying the effect of homogeneous and localized damage mechanisms on
632   the damping properties of damaged GFRP and CFRP continuous and woven composite laminates-an FEA
633   approach. Compos Part A Appl Sci Manuf 2005;36:367–79. doi:10.1016/j.compositesa.2004.06.037.

634 [57] Birman V, Byrd LW. Effect of matrix cracks on damping in unidirectional and cross-ply ceramic matrix
635   composites. J Compos Mater 2002;36:1859–77. doi:10.1177/0021998302036015247.

636 [58] Daneshjoo F, Gharighoran A. Experimental and theoretical dynamic system identification of damaged RC
637   beams. Electron J Struct Eng 2008;8:29–39.

638 [59] Panteliou SD, Chondros TG, Argyrakis VC, Dimarogonas AD. Damping factor as an indicator of crack
639   severity. J Sound Vib 2001;241:235–45. doi:10.1006/jsvi.2000.3299.